DBD Plasma Actuation on the Blades
of Axial-Flow Turbomachinery

David Greenblatt(✉) ⓘ, Omer Pfeffermann, and David Keisar ⓘ

Faculty of Mechanical Engineering, Technion – Israel Institute of Technology,
320003 Haifa, Israel
davidg@technion.ac.il

Abstract. Flow separation, or stall, in axial flow turbomachinery results in a loss of pressure or compression in the case of fans and compressors, or the loss of power or thrust generation in the case of turbines. Wave-power-based Wells turbines, in particular, suffer so acutely from blade stall during normal operation, that it compromises their viability as a major renewable energy resource. In this research, pulsed dielectric barrier discharge (DBD) plasma actuators were implemented on the blades of a mono-plane Wells turbine impeller and its full-bandwidth performance was evaluated. An initial parametric study indicated that blade-tip reduced frequencies ≥2.5 produced the greatest impeller acceleration from rest. The corresponding physical pulsation frequency was then used as a basis for conducting nominally steady-state experiments as well as experiments involving acceleration and deceleration of the impeller. Data so acquired, corresponding to a reduced frequency range of 0.9 to 2.5, was compiled to construct an impeller performance map. Plasma pulsations dramatically increased the effective impeller bandwidth by producing useful net power well beyond flow ratios where mono-plane impellers spin down to a standstill. In fact, the shaft power at a 17° blade-tip angle of attack exceeded the plasma input power by a factor of 33. These findings are potentially game-changing for wave energy generation and axial flow turbomachinery in general.

Keywords: Turbomachinery · Wave energy · Wells turbine · DBD plasma actuators · OWC turbine · Deep stall · Separation control

1 Introduction

Flow separation on the blades of rotating machinery, referred to as stall, severely limits their operational envelope, and can lead to high levels of vibration and in some cases, to damage or failure This is true for both incompressible-flow fans and compressors where the pressure or compressibility drop severely compromises the operation and safety of the machine [1–4]. Flow separation is also encountered in the low-pressure turbine stage of high-altitude unmanned air vehicles resulting in propulsion losses [5, 6]. Moreover, wave-power-based oscillating water column (OWC) turbines, eponymously named Wells turbines, in particular, suffer so acutely from blade stall throughout their normal operation, that it compromises their viability as a major renewable energy resource [7].

The simplifying assumptions associated with blade-element momentum theory [8] for incompressible or mildly compressible flows, allows the flow over a blade element (or section) to be viewed as analogous to that over an airfoil. While this is a significant simplification, it is nevertheless reasonable to posit that the inception and mechanism of stall over a blade element and airfoil are similar. By extension, active separation control methods that are effective on airfoils will also be effective on the blades of these axial-flow machines. This supposition can be used as a guiding principle for selecting and applying separation control methods.

The active separation control method selected for this research, is the single dielectric barrier discharge (DBD) plasma actuator [9]. There are three primary reasons for this selection. First, they effectively control separation on airfoils and wings throughout a large Reynolds and Mach number range (see references in [10]). Second, they have very low inertia and can easily withstand the centrifugal forces associated with high-speed rotation. Third, when pulse-modulated at low duty cycles, their electrical power consumption is low (typically watts/meter), which means that they can produce a net system benefit [11]. The axial-flow configuration selected presently for evaluating the efficacy of DBD plasma actuators is the Wells turbine impeller referred to above [12, 13]. Wells turbines convert hydraulic energy associated with undulating wave motion into an oscillating air column within an axial flow duct that houses the impeller. They present a particularly extreme and challenging environment because the conditions on the blades vary both temporally and spatially. Fixed-speed and fixed-geometry impellers cannot run efficiently in varying amplitude oscillatory duct flows and thus, during normal operation, the blade angles-of-attack vary between large positive and negative values leading to massive stall [13]. Indeed, Wells turbine stall produces such enormous power and bandwidth losses, noise and mechanical vibration, that it compromises their viability [14]. It therefore comes as no surprise that many techniques have been proposed to reduce or eliminate Wells turbine stall [15–24].

A proof-of-concept study performed by the present authors determined that pulse-modulated perturbations at dimensionless frequencies near unity produced enormous increases in post-stall Wells turbine performance and were effective at angles of attack up to 50° [25]. This reinforced our hypothesis that the excitation mechanism of separation control observed on airfoils and wings is also active on the rotating impeller blades. Furthermore, DBD plasma actuators can be configured to operate on both sides of the blades [26] and this renders them ideal for the oscillatory conditions experienced by the impeller.

The objective of this investigation is to characterize the performance of a Wells turbine impeller, throughout its operational range, when equipped with DBD plasma actuators. The axial-flow test facility described in [25], designed to accommodate blade-mounted DBD plasma actuators, was used to achieve this objective. The experimental facility, detailing the actuator implementation, measurement techniques and controlling parameters are described in Sect. 2. This is followed by a description of the methods employed and a discussion of the results in Sect. 3. Conclusions and future research are presented in Sect. 4.

2   Experimental Facility

The experimental facility (see Fig. 1) comprised a transparent air duct with an upstream bell-mouth contraction, an impeller assembly, and a 1.5 kW downstream suction fan (Soler and Palau HRT/4–500). The duct was made from three flanged 750 mm long acrylic tubes, with inner and outer radii of $R_i = 245$ mm and $R_o = 250$ mm respectively. The mono-plane impeller was comprised of a hub and six symmetric NACA 0015 blade profiles ($b = 140$ mm and $c = 100$ mm), that were 3D printed using ABS (Acrylonitrile Butadiene Styrene), resulting in a nominal solidity $\sigma = 0.5$. The hub diameter was 200 mm (thus tip and hub radii were $R_h = 100$ mm and $R_t = 240$ mm) with a half-ellipsoid nose fairing on the air inlet side. The blades were secured within slots at a 90° stagger angle between two (non-conducting Delrin and ABS) fore and aft rotating hub elements mounted on a Delrin shaft. The shaft was mounted on two bearings and the upstream part of the assembly was secured in place by three support rods, covered with a NACA 0015 fairings, at stagger angles of 0°.
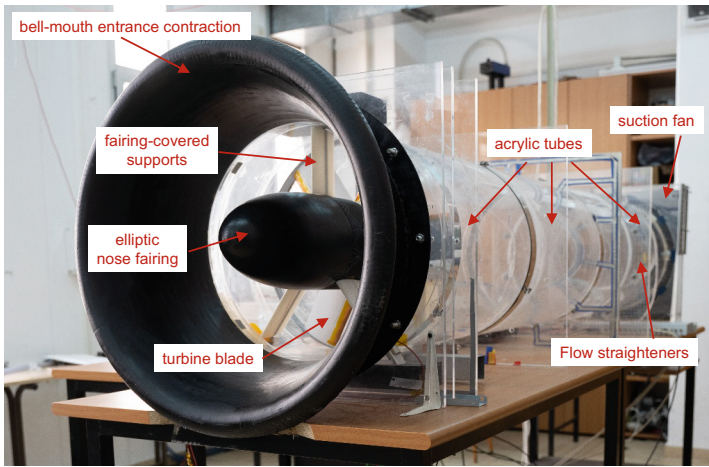

Fig. 1. Photograph of the axial flow facility from the air inlet side, showing the main externally visible components.

A photograph of the upstream part of the impeller assembly with the nose fairing removed (Fig. 2, left) shows the support-rod fairings and impeller blades, equipped with DBD plasma actuators. Also visible is an end-type slip-ring (Mercotac 215-2K) used to connect high voltage pulses to the DBD actuators. A photograph of the downstream part of the impeller assembly with the hub fairing removed (Fig. 2, right) shows the custom dynamometer, comprising a 1.0 Nm torque transducer (Kistler 4502A), a 1.0 Nm hysteresis brake (Magtrol HB-140), an optical speed (ω) sensor, and flexible couplings. A through-bore-type slip-ring (Prosper SRH3899) was mounted downstream of the impeller to serve as an earth for the plasma actuators.

The suction fan used to drive the system was accelerated to its design speed, namely 1,500 rpm, where the static pressure p_s versus volumetric flowrate Q characteristic curve
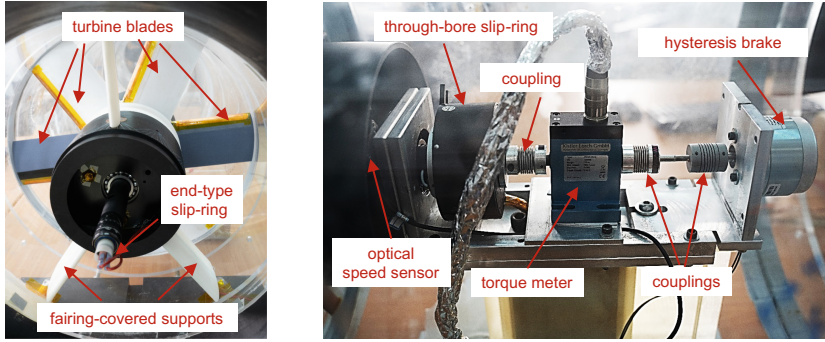
Fig. 2. Annotated photographs of: (left) the upstream part of the impeller with the nose faring removed; and (right) the downstream part of the impeller with the fairing removed.

was calibrated independently [25]. The axial velocity upstream of the impeller was thus calculated by simple conservation of mass, namely $U_x = 4Q/\pi(R_i^2 - R_h^2)$.

Each blade was printed with a leading-edge recess to accommodate the actuators that extended over the full span. The actuators were composed of a 20 mm wide $\times$ 20 µm thick copper electrode, encapsulated by a 300 µm thick translucent silicone rubber dielectric, and a 10 mm wide $\times$ 20µm thick exposed copper electrode. The actuators were driven in parallel by a modified Minipuls 2® high-voltage generator (GBS Elektronik GmbH) at $f_{ion} = 11,900$ Hz, using a CPX400D–Dual 420-W power supply. For the experiments presented herein, the actuators were pulse modulated at low duty cycles (d.c.) in the frequency range 60 Hz $\leq f_p \leq$ 400 Hz. Current (I) supplied to the Minipuls 2 was monitored by means of a Fluke 115 Digital Multimeter, thereby facilitating the gross power supplied to the actuator: $P_{in} = V_{DC}I$ (watts) [10]. Based on direct calibration [25], the net contribution of the pulsed plasma perturbations to the impeller torque was estimated to be $O(10^{-4})$ Nm.

3 Discussion of Results

3.1 Relevant Definitions

For the present implementation, the actuators were mounted along the entire span of the blades and therefore their pulse-modulation frequency f_p was fixed. Under the assumption of negligible radial and azimuthal velocity components, the magnitude of velocity relative to the blade can be written as:

$$W(r) = (U_x^2 + \omega^2 r^2)^{1/2} \tag{1}$$

and therefore, the nominal reduced frequency $F^+ = f_p c/W(r)$ varies along the span.

This should be contrasted with airfoils and H-bladed vertical axis wind turbines where the reduced frequency is constant along the span [27, 28]. For convenience, we define the nominal reduced frequencies at the tip ($U_t = \omega R_t$) and hub ($U_h = \omega R_h$), namely:

$$F_t^+ = \frac{f_p c}{U_t}(\varphi^2 + 1)^{-1/2} \tag{2}$$

and

$$F_h^+ = \frac{f_p c}{U_t} \frac{\zeta}{(\zeta^2 \varphi^2 + 1)^{1/2}} \tag{3}$$

for $U_t \neq 0$, where $\varphi \equiv U_x/U_t$ is the flow (or speed) ratio and $\zeta \equiv R_t/R_h$ is the tip-to-hub ratio. Similarly, the angles of attack at the tip and hub are expressed as $\alpha_t = \tan^{-1}(\varphi)$ and $\alpha_h = \tan^{-1}(\varphi\zeta)$.

Due to relatively large frictional torque caused by the bearings and slip-rings (common in laboratory-scale machines that produce $O(10^1)$ watts), we distinguish between the aerodynamic torque applied to the impeller T_A, the torque applied by the brake (torque meter reading) T_B and the frictional torque T_F. In this research, because T_F is non-negligible, the central objective is to determine T_A or, more specifically, the aerodynamic shaft power $P_A = T_A\omega$ throughout the turbine's operational range.

3.2   Effect of Modulation Frequency

In experiments performed previously [25], the suction fan was accelerated linearly to 1,500 rpm at an arbitrarily assigned time t_0, and the impeller was allowed to spin up and settle to a steady-state baseline condition, typically between 240 and 260 rpm. Under these conditions, the aerodynamic torque produced by the massively stalled blades was balanced by the friction in the slip-rings and bearings (see next section). The introduction of perturbations at $f_p \geq 200$ Hz caused the impeller to gradually speed up and continuously accelerate ($\dot{\omega} \equiv d\omega/dt > 0$). When the impeller speed reached 500 rpm, the perturbations were terminated, and the impeller spun down to its baseline values. This was done in order to remain within the design limits of the facility and avoid damage (see next section).

Due to small variations in initial conditions described above, for the present experiments, perturbations were initiated prior to accelerating the suction fan at t_0. The results of the impeller response and suction pressure, following a linear acceleration of the suction fan over 10 s, are shown in Fig. 3 and Fig. 4, respectively. For all cases, during spin-up of the suction fan (Fig. 4), the impeller is initially stationary (Fig. 3) with $F_t^+ = F_h^+ = F^+ = f_p c/U_x$ and starts rotating after 10–15 s. Over the next 20 s, all perturbation frequencies produce an improvement over the baseline steady-state case, but only frequencies of $f_p \geq 200$ Hz produced continuous acceleration of the impeller. In instances where the impeller reached 500 rpm, namely for the $f_p \geq 200$ Hz and 400 Hz cases, the fan was decelerated linearly to zero (indicated on the figures). In these experiments as well as those reported in [25], $f_p = 200$ Hz corresponds to $1.4 \leq F_t^+ \leq 2.5$ and this is well within the optimal reduced frequency range observed on airfoils [29, 30]. This further supports our conjecture that the instability mechanism operating on stationary airfoils is also active in the rotating frame. A new observation from the present data set is that perturbations are effective even at angles of attack as high as 90°.

The system pressure losses (Fig. 4) closely track the increases in rpm (or power) and facilitate the instantaneous calculation of Q from the fan curve, and hence fan power $P_{\text{fan}} = -p_s Q$ and net impeller aerodynamic efficiency $\eta = (P_A - P_{\text{in}})/P_{\text{fan}}$. An unexpected result was that following deceleration of the fan under $f_p = 200$ Hz and
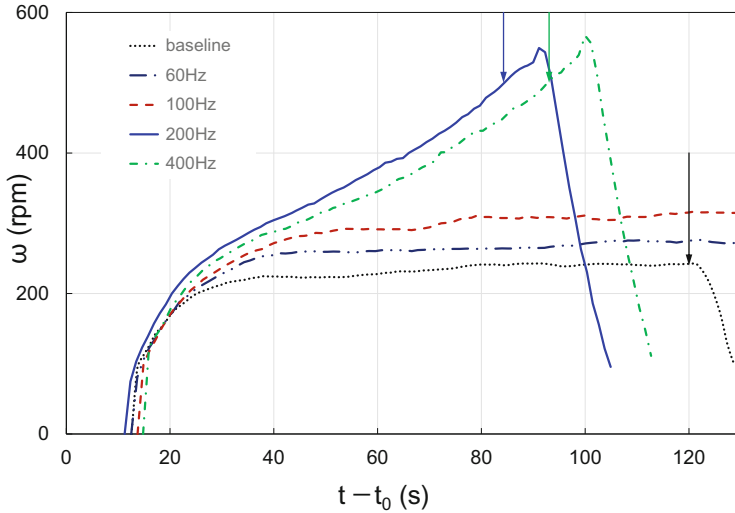
Fig. 3. Impeller rotational speed-up resulting from acceleration (from $t_0 = 0$) and deceleration of the suction fan for the uncontrolled (baseline) and different perturbation frequencies (see corresponding suction pressure in Fig. 4). The fan accelerates and decelerates linearly over 10 s. Vertical arrows indicate the initiation of fan deceleration.

400 Hz perturbations (see indications in Fig. 3 and Fig. 4), the impeller *accelerated* for approximately 7 s. In contrast, following fan deceleration in the baseline case, the speed remained constant for 1.5 s following deceleration of the fan and then spun down. This intriguing observation can be explained as follows. At $\omega = 500$ rpm, the flow ratio $\varphi = 0.56$, the tip angle of attack $\alpha_t = 29°$ and hence the impeller is deeply stalled. Under these conditions, the reduced frequencies at the tip are $F_t^+ = 1.4$ and 2.8. As the fan decelerates, U_x decreases and therefore, so do φ and α. For example, when U_x halves its value, the blades experience light (or shallow) stall conditions, corresponding to $\varphi = 0.28$ and $\alpha_t = 16°$. And because pulsed perturbations are particularly effective within this regime on airfoils at $F_t^+ = 0.7$ and 1.4, the aerodynamic efficiency (C_L/C_D) of the blades increases dramatically. We again implicitly assert that even though the conditions vary spatially and temporally on the blades, the separated shear layer excitation mechanism active on airfoils is also active on the rotating blades. Indeed, this improvement is so dramatic that the impeller accelerates even though the dynamic pressure relative to the blade, namely $^1/_2\rho(U_t^2 + U_x^2)$, decreases.

3.3 Overall Turbine Performance

One difficulty associated with controlling the massive stall conditions described in the previous section was that the turbine speed could not easily be maintained constant. This is because the perturbations increased impeller speed, corresponding to lower angles of attack and hence greater flow control effectiveness [10]. Hence, the impeller not only sped up, but the rate of speed-up also increased. Lightly loading the impeller with the hysteresis brake (<100 Nmm) led to a more gradual acceleration of the impeller, while
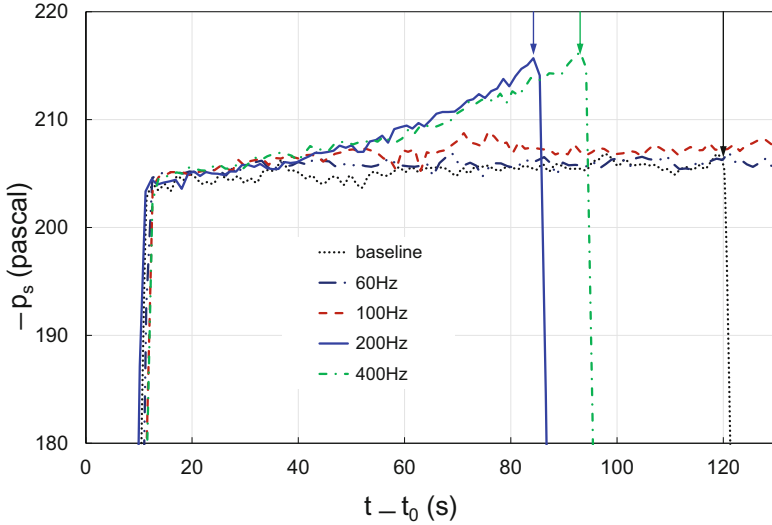
Fig. 4. Suction pressure produced in the tube following acceleration (from $t_0 = 0$) and deceleration of the fan for the uncontrolled (baseline) and different perturbation frequencies (see corresponding impeller speed in Fig. 3). The fan accelerates and decelerates linearly over 10 s. Vertical arrows indicate the initiation of fan deceleration.

slightly higher loading (>100 Nmm), produced deceleration and a lower settling speed. Although closed-loop control can be used to attain a set-point for the machine, this was considered to be outside of the objectives of this paper. Instead, we conducted a series of experiments under accelerating and deceleration conditions. We then used a composite of these experiments to construct a performance map.

To account for all of the combinations mentioned above, the unsteady system equation must be considered, namely:

$$J_0 \dot{\omega} = T_A - T_B - T_F \tag{4}$$

Hence with the shaft nominally unloaded and rotating at a constant speed, the aerodynamic torque is balanced by the frictional torque as described in the previous section. Our objective here is to quantify T_A and hence determine the aerodynamic shaft power $P_A = T_A \omega$ under all operational conditions.

In order to determine the non-negligible frictional torque due to the slip-rings and bearings, the simplified form of Eq. (4), namely $\dot{\omega} = T_F/J_0$ was employed. To determine $\dot{\omega}$ under frictional loading alone, namely under the conditions $U_x = 0$, the impeller was spun up to 500 rpm, after which the fan was decelerated to zero, and the perturbations were terminated. The impeller was then allowed to spin down to zero under quiescent conditions ($U_x = 0$) to obtain $\omega = \omega(t)$. These experiments were performed periodically throughout the experimental campaign and a data sample is shown in Fig. 5, where the deceleration is referenced to arbitrary time t'. Linear least-squares curves were fitted to the data and an average was used to determine $\dot{\omega} = -3.66$ rad/s^2. In order to determine J_0, the individual components of the impeller (hub, bearings, slip-rings

and blades) were weighed and then $J_0 = 0.050$ kg m^2 was calculated based on the geometric configuration of the impeller assembly. Finally, the frictional torque, namely $T_F = J_0\dot{\omega} = -0.183$ Nm, was determined and considering that the maximum brake torque was 1 Nm, friction comprised a sizeable fraction of the overall load.
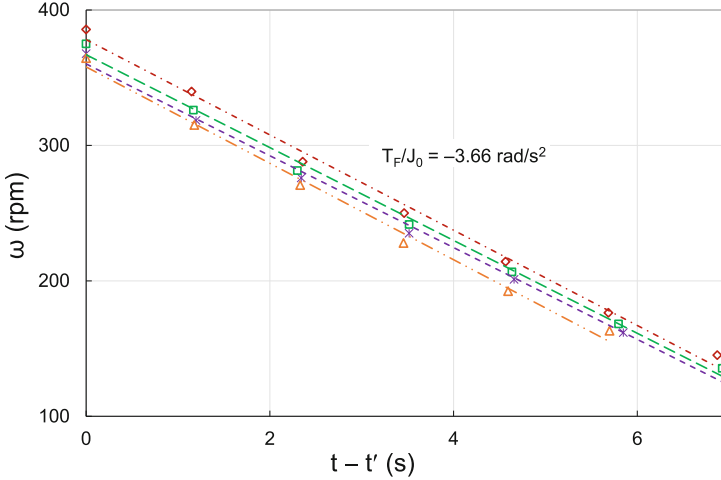

Fig. 5. Representative data sets acquired throughout the experimental campaign, illustrating spin-down of the impeller under frictional loading alone.

In an attempt to attain constant impeller speeds, two separate experiments were performed. The first illustrates the effect of spinning up the turbine and then terminating the plasma perturbations, while the second shows the effect of braking the turbine while the plasma perturbations are active. In the first experiment, the impeller was allowed to speed-up, and then the brake was set close to its maximum setting (Fig. 6). This resulted in a gradual deceleration until the pulsations were terminated, following which the impeller spun down to a standstill. The clearest evidence that the perturbations are responsible for driving the turbine is that the turbine immediately and rapidly spins down when they are terminated. For this experiment, the aerodynamic torque was determined in the region of constant torque with perturbations activated, where $\dot{\omega}$ was estimated by a least-squares curve fit.

In the second experiment, a lower brake setting was employed, resulting in a near constant rotational speed (Fig. 7). A subsequent increase in loading brought the impeller to a standstill. In this experiment, two relevant data were extracted. The first was based on average values between 120 and 150 s under the assumption that $\dot{\omega} = 0$. The aerodynamic shaft power, namely 82 W (Eq. 4), is slightly higher than the estimate in [25] and is achieved with a plasma input power of 2.5 W, representing an astonishing ratio $P_A/P_{in} = 33$. An accumulation of previous experience on airfoils [10, 29] shows that as the post stall angle is reduced, the separation control effect increases. Nevertheless, this remains an extraordinary result in light of the fact that the angle-of-attack varies from 17° to 30° from tip to hub. The second relevant data were extracted from the deceleration phase where $\omega(t)$ was determined using a fourth-order polynomial curve-fit.
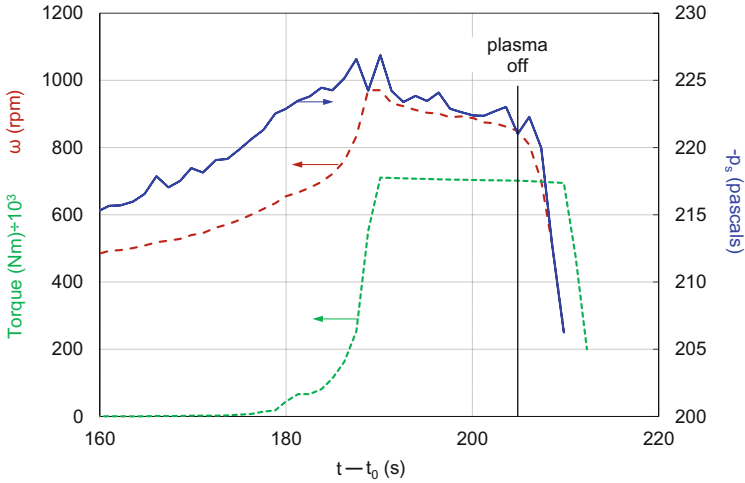
Fig. 6. Impeller rotational speed, system pressure loss and torque for the loaded turbine with plasma pulsations at $f_p = 200\,\text{Hz}$ and d.c. $= 1.7\%$. Arrows indicate axis corresponding to the data set.

The final experiment in this series involved unloading the turbine and allowing it to accelerate under the braking effect of friction alone. Although this experiment exceeded the design load of the blades, it was deemed critical to obtaining the turbine performance over a larger bandwidth. The results from this experiment (Fig. 8) show both ω and $\dot{\omega}$ initially increasing. At approximately 96 s, corresponding to 80 rad/s or 760 rpm, the impeller accelerated dramatically, reached inflection 99 s, and continued to accelerate ($\dot{\omega} > 0$) until a blade failed. Under these conditions, the $\dot{\omega}$ term dominates as shown in the figure and the aerodynamic torque is calculated according to $T_A = J_0\dot{\omega} + T_F$.

The data extracted from Fig. 6, Fig. 7 and Fig. 8 are summarized on the performance map shown in Fig. 9. The steady-state and mild deceleration data are indicated as solid symbols and the acceleration and deceleration phases are shown by open symbols. Error bars indicate uncertainty resulting from differentiation of the experimental data. Despite the disparate methods employed for accumulating these data, they amalgamate to produce a consistent map that clearly reveals the effects of pulsed plasma perturbations. In the relatively low flow ratio range, namely $\varphi \leq 0.22$ range ($\alpha_t \leq 13°$), corresponding to values below which the peak power occurs, it is not clear if perturbations produce a positive gross net effect because no baseline data is available. Here the peak aerodynamic efficiency $\eta = (P_A - P_{in})/P_{fan}$ is 48.5%. This is somewhat lower than values around 65% cited in the literature [13] and is most likely due to the relatively low tip Reynolds numbers that peak at 2.4×10^5. At flow ratios greater than some critical value, conventional impellers produce zero power. For example, comparable solidity ($\sigma = 0.51$) mono-plane impellers [13], stall at $\varphi \geq 0.24$, resulting in a total shut-down of power generation with accompanying noise and potentially destructive vibrations. In our experiments, the critical value falls between 0.22 and 0.29 above which plasma pulsations always produce net positive aerodynamic efficiency $\eta = (P_A - P_{in})/P_{fan}$. This has a dramatic effect on the turbine bandwidth and this factor alone has the potential
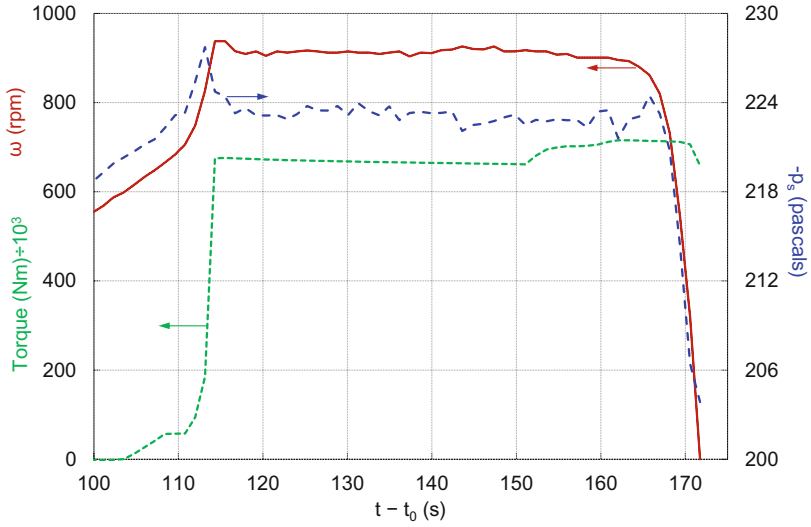
Fig. 7. Impeller rotational speed under increasing load until spin-down with plasma pulsations at $f_p = 200$ Hz and d.c. $= 1.7\%$. Arrows indicate axis corresponding to the data set.
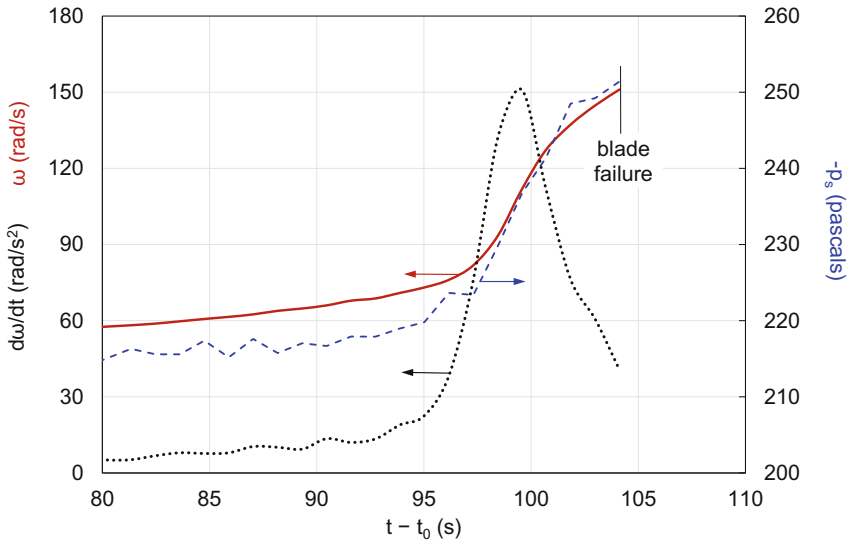

Fig. 8. Impeller speed and acceleration to failure, together with fan pressure, under frictional loading with pulsations at $f_p = 200$ Hz and d.c. $= 1.7\%$. Arrows indicate axis corresponding to the data set.

to dramatically increase the overall efficiency of Wells turbines. A question still open is whether perturbations increase peak power values, and this should be a topic for future research.
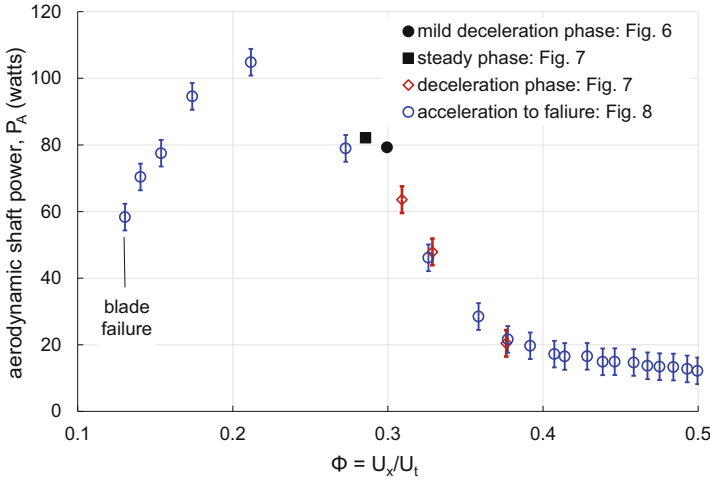

Fig. 9. Amalgamation of data acquired to construct a Wells turbine performance map in the presence of plasma pulsations at $f_p = 200$ Hz.

In the present experiments with $f_p = 200$ Hz, the reduced frequency range varies from $F_t^+ = 2.5$ under fully stalled stationary conditions ($\alpha_t = 90°$) to $F_t^+ = 0.9$ under incipient stall conditions ($\alpha_t = 12°$) corresponding to the peak in Fig. 9. As hypothesized previously, the most probably reason why $f_p = 200$ Hz pulsations consistently produce the most favorable results is that the corresponding reduced frequency range falls well within range known to be effective on airfoils, namely $0.5 \leq F^+ \leq 3$ [29, 30]. These frequencies are effective at generating nearly two-dimensional spanwise vortices that deflect the shear layer towards the airfoil surface, thereby increasing lift. Despite the loss of two-dimensionality along the blade span of the impeller, this mechanism still appears to be highly effective.

The present proof-of-concept study focused on performance measurements and, although tremendous potential was demonstrated, a number of topics are suggested for future research. First, although it was hypothesized that the inception and mechanism of stall over blades and airfoils are similar, this was not directly validated. In future studies, blade surface pressure measurements, as well as optical flow-field measurements, must be performed to gain an understanding of the blade aerodynamics. Second, our experiments were performed under laboratory-scale conditions, where the maximum tip Reynolds numbers ($\leq 2.4 \times 10^5$) were an order of magnitude smaller than those on in-service machines. Thus, a large test facility should be developed to evaluate the viability of plasma actuators under full-scale conditions. If the blade-airfoil analogy is indeed valid, then effective airfoil separation control shown by [31] at $Re > 2 \times 10^6$ (Mach number of 0.4) bodes well for full-scale applications. The main caveat is that the

plasma body force per unit width must scale with the tip dynamic pressure and chord, namely $^1/_2\rho(U_x^2 + U_t^2)c$ and this may require different high voltage generators [32] to those employed here. Third, another DBD technology that may also have significant potential for controlling blade separation due to its effectiveness on airfoils is pulsed-periodic nanosecond excitation [33]. Pulses of $O(10^1)$ nanoseconds can produce $O(1)$ microsecond overheating of several hundred degrees within the discharge region. Periodic pulses thus produce a series of compression waves and in this sense the mechanism of pulsed-periodic nanosecond excitation is different from that employed presently.

4   Conclusions and Future Research

The present investigation studied the effect of pulsed DBD plasma actuators on Wells turbine impeller performance throughout its operational range. Experiments were conducted initially to isolate the most effective pulsation frequency without biasing the data with different initial conditions. A pulsation frequency of $f_p = 200$ Hz, corresponding to $F^+ = 2.5$ under massively stalled conditions produced the greatest acceleration of the impeller. This physical frequency was then used as a basis for conducting nominally steady-state experiments as well as experiments involving acceleration and deceleration of the impeller. The unsteady equation of rotary motion was used, in conjunction with the experimental data, to construct the impeller performance map.

The most significant steady-state result indicated an aerodynamic shaft power of 82 W at a tip angle of attack of 17°, which, remarkably, was 33 times higher than the plasma input power. Decelerating the impeller under these conditions, in conjunction with the equation of motion, revealed the deep-stall benefits of plasma perturbations. On the other hand, accelerating the impeller to destruction under frictional loads alone, again in conjunction with the equation motion, allowed characterization of virtually the entire operational range. The dramatic increase in the operational bandwidth shows that DBD plasma actuators have the potential to be a game-changing OWC technology. Positive implications for axial flow fans, compressors and low-pressure turbine stages can also clearly be extrapolated. The reduced frequency at the tip varied between 0.9 and 2.5 in the post-stall regime, which fell well within the effective excitation range on two-dimensional airfoils. Thus, the excitation mechanism still appears to be highly effective on the blades despite the loss of flow two-dimensionality.

Future research should focus on understanding the aerodynamics of the problem and evaluating DBD plasma effectiveness at higher Reynolds numbers. Furthermore, an oscillatory bi-directional-flow facility, representative of Wells turbine operational conditions, should be constructed. Application of DBD plasma actuators under these oscillatory conditions will provide a clearer evaluation of overall system benefits. Such a system should also include some form of closed-loop control with sensors for flow direction and incipient stall, with the ability to initiate and terminate perturbations [11, 34] on the appropriate stalling surface [26].

References

1. de Jager, B.: Rotating stall and surge control: a survey. In: Proceedings of the IEEE Conference on Decision and Control. pp. 1857–1862. IEEE (1995). https://doi.org/10.1109/cdc.1995.480612

2. Sheard, A.G., Corsini, A.: The mechanical impact of aerodynamic stall on tunnel ventilation fans. Int. J. Rotating Mach. **2012**, 1–12 (2012). https://doi.org/10.1155/2012/402763

3. Bianchi, S., Corsini, A., Sheard, A.G., Tortora, C.: A critical review of stall control techniques in industrial fans (2013). https://doi.org/10.1155/2013/526192

4. Greitzer, E.M.: Axial compressor stall phenomena. J. Fluids Eng. Trans. ASME. **102**, 134–151 (1980). https://doi.org/10.1115/1.3240634

5. Huang, J., Corke, T.C., Thomas, F.O.: Plasma actuators for separation control of low-pressure turbine blades. AIAA J. **44**, 51–57 (2006). https://doi.org/10.2514/1.2903

6. Hultgren, L.S., Ashpis, D.E.: Demonstration of separation control using dielectric barrier discharge plasma actuators. AIAA J. **56**, 4614–4620 (2018). https://doi.org/10.2514/1.J056976

7. QUB: Islay LIMPET wave power plant. Contract JOR3-CT98–0312 (2002)

8. Dixon, S.L.: Fluid mechanics, thermodynamics of turbomachinery (1975). https://doi.org/10.1016/0017-9310(77)90019-9

9. Corke, T.C., Post, M.L., Orlov, D.M.: SDBD plasma enhanced aerodynamics: concepts, optimization and applications (2007). https://doi.org/10.1016/j.paerosci.2007.06.001.

10. Keisar, D., Hasin, D., Greenblatt, D.: Plasma actuator application on a full-scale aircraft tail. AIAA J. **57**, 616–627 (2019). https://doi.org/10.2514/1.J057233

11. Ben-Harav, A., Greenblatt, D.: Plasma-based feed-forward dynamic stall control on a vertical axis wind turbine. Wind Energy **19**, 3–16 (2016). https://doi.org/10.1002/we.1814

12. Antonio, F.D.O.: Wave energy utilization: A review of the technologies (2010). https://doi.org/10.1016/j.rser.2009.11.003

13. Raghunathan, S.: The wells air turbine for wave energy conversion (1995). https://doi.org/10.1016/0376-0421(95)00001-F

14. Boake, C.B., Whittaker, T.J.T., Folley, M., Ellen, H.: Overview and initial operational experience of the LIMPET wave energy plant. In: Proceedings of the International Offshore and Polar Engineering Conference, pp. 586–594 (2002)

15. Setoguchi, T., Santhakumar, S., Takao, M., Kim, T.H., Kaneko, K.: Effect of guide vane shape on the performance of a Wells turbine. Renew. Energy. **23**, 1–15 (2001). https://doi.org/10.1016/S0960-1481(00)00163-4

16. Amundarain, M., Alberdi, M., Garrido, A.J., Garrido, I., Maseda, J.: Wave energy plants: Control strategies for avoiding the stalling behaviour in the Wells turbine. Renew. Energy. **35**, 2639–2648 (2010). https://doi.org/10.1016/j.renene.2010.04.009

17. Lekube, J., Garrido, A.J., Garrido, I., Otaola, E., Maseda, J.: Flow control in wells turbines for harnessing maximum wave power. Sensors (Switzerland) **18**, 535 (2018). https://doi.org/10.3390/s18020535

18. Mishra, S., Purwar, S., Kishor, N.: Maximizing output power in oscillating water column wave power plants: an optimization based MPPT algorithm. Technologies. **6**, 15 (2018). https://doi.org/10.3390/technologies6010015

19. Halder, P., Samad, A., Thévenin, D.: Improved design of a Wells turbine for higher operating range. Renew. Energy. **106**, 122–134 (2017). https://doi.org/10.1016/j.renene.2017.01.012

20. Gato, L.M.C., Webster, M.: An experimental investigation into the effect of rotor blade sweep on the performance of the variable-pitch Wells turbine. Proc. Inst. Mech. Eng. Part A J. Power Energy **215**, 611–622 (2001). https://doi.org/10.1243/0957650011538848

21. M'zoughi, F., Bouallègue, S., Ayadi, M., M'zoughi, F., Garrido, A.J., Garrido, I.: Modelling and airflow control of an oscillating water column for wave power generation. In: 2017 4th International Conference on Control, Decision and Information Technologies, CoDIT 2017, pp. 938–943. Institute of Electrical and Electronics Engineers Inc. (2017). https://doi.org/10.1109/CoDIT.2017.8102718

22. Gato, L.M.C., Eça, L.R.C., De, A.F.: Performance of the wells turbine with variable pitch rotor blades. J. Energy Resour. Technol. Trans. ASME. **113**, 141–146 (1991). https://doi.org/10.1115/1.2905794

23. Shehata, A.S., Xiao, Q., Selim, M.M., Elbatran, A.H., Alexander, D.: Enhancement of performance of wave turbine during stall using passive flow control: First and second law analysis. Renew. Energy. **113**, 369–392 (2017). https://doi.org/10.1016/j.renene.2017.06.008

24. Das, T.K., Samad, A.: Influence of stall fences on the performance of Wells turbine. Energy **194**, 116864 (2020). https://doi.org/10.1016/j.energy.2019.116864

25. Greenblatt, D., Pfeffermann, O., Keisar, D., Göksel, B.: Wells turbine stall control using plasma actuators. AIAA J. **59**, 765–772 (2021). https://doi.org/10.2514/1.J060278

26. Greenblatt, D., Lautman, R.: Inboard/outboard plasma actuation on a vertical-axis wind turbine. Renew. Energy. **83**, 1147–1156 (2015). https://doi.org/10.1016/j.renene.2015.05.020

27. Greenblatt, D., Schulman, M., Ben-Harav, A.: Vertical axis wind turbine performance enhancement using plasma actuators. Renew. Energy. **37**, 345–354 (2012). https://doi.org/10.1016/j.renene.2011.06.040

28. Greenblatt, D., Ben-Harav, A., Mueller-Vahl, H.: Dynamic stall control on a vertical-axis wind turbine using plasma actuators. AIAA J. **52**, 456–462 (2014). https://doi.org/10.2514/1.J052776

29. Greenblatt, D., Wygnanski, I.: The control of flow seperation by periodic excitation. Prog. Aerosp. Sci. **36**, 487–545 (2000). https://doi.org/10.1016/S0376-0421(00)00008-7

30. Greenblatt, D., Göksel, B., Rechenberg, I., Schüle, C.Y., Romann, D., Paschereit, C.O.: Dielectric barrier discharge flow control at very low flight Reynolds numbers. AIAA J. **46**, 1528–1541 (2008). https://doi.org/10.2514/1.33388

31. Kelley, C.L., et al.: High Mach number leading-edge flow separation control using AC DBD plasma actuators. In: 50th AIAA Aerospace Sciences Meeting Including the New Horizons Forum and Aerospace Exposition (2012). https://doi.org/10.2514/6.2012-906

32. Thomas, F.O., Corke, T.C., Iqbal, M., Kozlov, A., Schatzman, D.: Optimization of dielectric barrier discharge plasma actuators for active aerodynamic flow control. AIAA J. **47**, 2169–2178 (2009). https://doi.org/10.2514/1.41588

33. Roupassov, D.V., Nikipelov, A.A., Nudnova, M.M., Starikovskii, A.Y.: Flow separation control by plasma actuator with nanosecond pulsed-periodic discharge. AIAA J. **47**, 168–185 (2009). https://doi.org/10.2514/1.38113

34. Greenblatt, D., Neuburger, D., Wygnanski, I.: Dynamic stall control by intermittent periodic excitation. J. Aircr. **38**, 188–189 (2001). https://doi.org/10.2514/2.2751